

# Probing topological phase transitions using high-harmonic generation

Christian Heide<sup>1,2,7</sup>✉, Yuki Kobayashi<sup>1,2,7</sup>, Denitsa R. Baykusheva<sup>3</sup>, Deepti Jain<sup>4</sup>, Jonathan A. Sobota<sup>5</sup>, Makoto Hashimoto<sup>6</sup>, Patrick S. Kirchmann<sup>5</sup>, Seongshik Oh<sup>4</sup>, Tony F. Heinz<sup>1,2</sup>, David A. Reis<sup>1,2</sup> and Shambhu Ghimire<sup>1</sup>✉

**The prediction and realization of topological insulators have sparked great interest in experimental approaches to the classification of materials<sup>1-3</sup>. The phase transition between non-trivial and trivial topological states is important, not only for basic materials science but also for next-generation technology, such as dissipation-free electronics<sup>4</sup>. It is therefore crucial to develop advanced probes that are suitable for a wide range of samples and environments. Here we demonstrate that circularly polarized laser-field-driven high-harmonic generation is distinctly sensitive to the non-trivial and trivial topological phases in the prototypical three-dimensional topological insulator bismuth selenide<sup>5</sup>. The phase transition is chemically initiated by reducing the spin-orbit interaction strength through the substitution of bismuth with indium atoms<sup>6,7</sup>. We find strikingly different high-harmonic responses of trivial and non-trivial topological surface states that manifest themselves as a conversion efficiency and elliptical dichroism that depend both on the driving laser ellipticity and the crystal orientation. The origins of the anomalous high-harmonic response are corroborated by calculations using the semiconductor optical Bloch equations with pairs of surface and bulk bands. As a purely optical approach, this method offers sensitivity to the electronic structure of the material, including its nonlinear response, and is compatible with a wide range of samples and sample environments.**

The discovery of three-dimensional topological insulators and subsequent advances in materials engineering have attracted enormous attention in the materials research community<sup>1-3</sup>. One of the most salient properties of topological insulators is the presence of a conducting, gapless surface state that is protected by time-reversal symmetry, as shown in the inset of Fig. 1a. This state is a consequence of the band inversion in the bulk material from strong spin-orbit coupling<sup>8-10</sup>. The surface bands are spin-polarized, which suppresses backscattering from disorder and non-magnetic impurities and allows for spin currents<sup>4</sup>. These properties offer a promising platform for many applications ranging from dissipation-free charge transport to spin-based light-wave electronics and fault-tolerant quantum computing<sup>2,4,11</sup>.

Probing topological phase transitions is a major challenge in materials research<sup>12-15</sup>. Spin- and angle-resolved photoelectron spectroscopy (or s-ARPES) has long been the workhorse technique for probing topologically protected surface states of bulk solids<sup>16</sup>. In

this method, the electrons are photo-emitted from the sample, and their energy, momentum and spin polarization are analysed as they reach the detector. This requires ultrahigh vacuum conditions and a clean surface.

Here we demonstrate a novel all-optical approach based on circularly polarized laser-field-driven high-harmonic generation (HHG)<sup>5</sup> to probe topological phase transitions. This method is compatible with a wide range of samples and sample environments, including buried interfaces, heterostructures, microelectronics and flexible electronics. In our experiments we examine the prototypical topological insulator bismuth selenide ( $\text{Bi}_2\text{Se}_3$ ), whose electronic band structure and associated transport properties have been well characterized (see Extended Data Fig. 1 and refs. <sup>3,6,7</sup>).

HHG has been studied extensively using atomic and molecular targets<sup>17</sup>. One of its remarkable features is its structural sensitivity, which arises from the underlying re-scattering mechanism and enables ångström-scale probing of the electronic wavefunction of an aligned target molecule<sup>18</sup>. The extension of high-harmonic spectroscopy to solid materials presents the important possibility of the all-optical probing of ångström-scale valence charge distributions in real space<sup>19,20</sup> and of the electronic band structure in momentum space<sup>21</sup>, including signatures of the Berry curvature<sup>22,23</sup>. In terms of the possibilities of probing topological phase transitions, Bauer and Hansen<sup>24</sup> have predicted theoretically, using a one-dimensional model system, that the topologically protected edge states lead to highly efficient HHG. Silva et al.<sup>25</sup> and Chacón et al.<sup>26</sup> independently predicted, using a two-dimensional Haldane model system, that the topological invariants can be obtained by analysing the helicity of high-order harmonics.

Recently, HHG has been realized experimentally in three-dimensional topological insulators, showing even-order harmonics<sup>27,28</sup> as well as an anomalous ellipticity dependence<sup>29</sup>, which has been assigned to the contribution of topologically protected surface states. In the present work we study the high-harmonic response of chemically substituted  $(\text{Bi}_{1-x}\text{In}_x)_2\text{Se}_3$  for different compositions  $x$ . According to angle-resolved photoelectron spectroscopy (ARPES) and transport studies, shown in Extended Data Fig. 1 and in ref. <sup>6</sup>, at around  $x \approx 7-10\%$  the phase transition from a topologically non-trivial state to a topologically trivial state occurs. At around 20% the topological surface states disappear completely. We find that the crystal-orientation and the laser-ellipticity dependence of the HHG radiation emitted from pristine  $\text{Bi}_2\text{Se}_3$  and

<sup>1</sup>Stanford PULSE Institute, SLAC National Accelerator Laboratory, Menlo Park, CA, USA. <sup>2</sup>Department of Applied Physics, Stanford University, Stanford, CA, USA. <sup>3</sup>Department of Physics, Harvard University, Cambridge, MA, USA. <sup>4</sup>Center for Quantum Materials Synthesis and Department of Physics & Astronomy, Rutgers, The State University of New Jersey, Piscataway, NJ, USA. <sup>5</sup>Stanford Institute for Materials and Energy Sciences, SLAC National Accelerator Laboratory, Menlo Park, CA, USA. <sup>6</sup>Stanford Synchrotron Radiation Lightsource, SLAC National Accelerator Laboratory, Menlo Park, CA, USA. <sup>7</sup>These authors contributed equally: Christian Heide and Yuki Kobayashi. ✉e-mail: [cheide@stanford.edu](mailto:cheide@stanford.edu); [shambhu@stanford.edu](mailto:shambhu@stanford.edu)

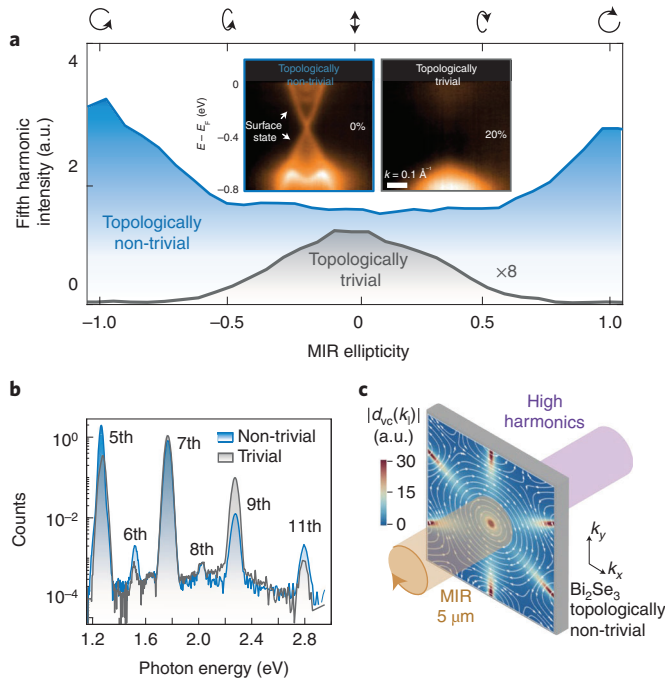


**Fig. 1 | Probing topological phase transitions using HHG.** **a**, Inset: measured band structure using ARPES, showing the topologically protected surface state for the pure  $\text{Bi}_2\text{Se}_3$  sample (left), which vanishes for high indium concentration (right). The intensity of the fifth harmonic as a function of the MIR ellipticity is measured for both phases. Strong high-harmonic enhancement is observed for the topologically non-trivial sample, especially for circular excitation. Note that intensity of the topologically trivial sample has been up-scaled by a factor of 8. **b**, Measured high-harmonic spectrum for both phases, under linear excitation (blue: topologically non-trivial, black: topologically trivial). Odd- and even-order harmonics are observed for both phases. **c**, Dipole matrix element  $d_{vc}$  along the in-plane momentum  $k_{\parallel}$  connecting the lower and the upper part of the Dirac cone. The color quantifies the absolute magnitude of  $d_{vc}(k_{\parallel})$ , with an enhanced amplitude in the vicinity of the Dirac point and the real parts of the x- and the y-components are visualized as a vector field (white arrows), giving rise to a helical vortex structure. Both, the enhanced amplitude and the helical vortex structure are related to an increase of the HHG under circular excitation. See Supplementary Information for intraband contributions.

$(\text{Bi}_{0.8}\text{In}_{0.2})_2\text{Se}_3$  are markedly different, including in their elliptical dichroism.

In our experiments, we use ultrashort laser pulses with a central wavelength of  $5\ \mu\text{m}$ , which corresponds to a photon energy well below the bulk bandgap of  $\text{Bi}_2\text{Se}_3$  ( $\sim 0.3\ \text{eV}$ ). The measurements are performed in transmission geometry with normally incident laser excitation under ambient conditions. To ensure that our experiments probe two limits in the topological phase diagram, we compare two extreme cases: topologically non-trivial ( $x=0$ ) and topologically trivial ( $x=0.2$ ) states of the material. In Extended Data Figs. 1 and 2 we show the results for intermediate doping concentrations. For a vacuum peak electric field strength of  $E_0=0.21\ \text{V nm}^{-1}$  (vacuum peak intensity  $I_0=5.4\times 10^{10}\ \text{W cm}^{-2}$ ), we observe even- and odd-order harmonics, ranging from the fifth to the eleventh harmonic order from both samples, as shown in Fig. 1b.

Apart from the higher efficiency for the fifth and sixth harmonic order, no clear difference between the two distinct topological phases is observed under linear polarization. In particular, even-order harmonics are observed for both samples. Our results

suggest that observing even-order harmonics is a consequence of a broken inversion symmetry at the surface, as depicted in Fig. 2a,b, but not necessarily a clear signature of non-trivial topology<sup>27,28,30,31</sup>. A robust connection with topological properties can, however, be demonstrated via the consideration of additional observables, such as the response of the material to circularly polarized laser fields<sup>5,29</sup>.

Figure 1a shows the high-harmonic intensity of the fifth harmonic for various values of the mid-infrared (MIR) ellipticity  $\varepsilon$ . We find that for the topologically trivial sample, the high-harmonic intensity is maximized for  $\varepsilon=0$  (linearly polarized) and drops monotonically as the ellipticity increases to  $\varepsilon=\pm 1$ . For circular polarization, we detect no high-harmonic response (grey line). By contrast, the topologically non-trivial sample shows strikingly different behaviour (blue line): higher absolute high-harmonic yield ( $\sim 10$ ), which grows with increasing laser ellipticity. For  $\varepsilon=\pm 1$  the high-harmonic yield is about twice as high as for  $\varepsilon=0$ . In Extended Data Fig. 2 we show the ratio of the high-harmonic intensities generated via circularly polarized ( $I_{\text{HH,C}}$ ) versus linearly polarized ( $I_{\text{HH,L}}$ ) excitation, which is also denoted as  $\mathcal{R}$  (see later). In the case of topologically non-trivial samples ( $x<0.08$ ), we find that the high-harmonic response under circular excitation dominates that under linear excitation.

Systematic measurements of the intensities of the fifth and sixth harmonics for various MIR ellipticities and sample orientations are shown for both samples (topologically non-trivial in Fig. 2d and topologically trivial in Fig. 2e). Owing to the three-fold rotational symmetry of the crystal (Fig. 2c), we limit our discussion to the crystal angles  $\phi=-30^\circ$  to  $+30^\circ$ . Here,  $\phi=\pm 30^\circ$  corresponds to the condition when the polarization vector of the laser field is orthogonal to the mirror plane (parallel:  $\phi=0^\circ$ ; see Fig. 2).

Again, we observe that under circular MIR excitation, the fifth harmonic shows the highest high-harmonic intensity, which is in contrast to the topologically trivial sample. For the sixth harmonic order, the maximal yield is observed for elliptically polarized excitation  $\varepsilon\approx\pm 0.4$ . Based on dynamical symmetries, HHG for exactly circular polarization for this harmonic order is prohibited<sup>13,32</sup>.

To reproduce the complex pattern of  $\phi$  versus  $\varepsilon$  and understand the anomalous ellipticity dependence, we extend our model simulations reported previously<sup>7</sup> to crystal angles from  $\phi=-30^\circ$  to  $+30^\circ$ . We model the response of the topological surface states using a pair of gapless (Dirac-like) states, whereas the emission from the trivial doped compound is calculated based on a pair of gapped valence and conduction bands. The numerical results are plotted in Fig. 2d (bottom plots) for the fifth and sixth harmonic orders. Apart from some deviations around  $\phi=0^\circ$ , our calculations not only reproduce quantitatively the ratio of the HHG yield under linear and circular excitation for the fifth harmonic, but also capture the basic features of the rather complex ellipticity dependence. For example, the decreased high-harmonic yield for the fifth harmonic under elliptical excitation and a crystal axis angle of  $\pm 30^\circ$ , as well as the reduced yield for the sixth harmonic for linear excitation, are reproduced by the simulations.

By contrast, the calculated harmonic efficiency from the bulk bands (shown in the Supplementary Information) decreases monotonically with increasing laser ellipticity, which is in agreement with the experimental results for doped samples, without the topologically protected surface states.

The good agreement between simulation and measurement enables us to attribute this enhancement principally to two factors, as depicted in Fig. 1c for the interband harmonics (see Supplementary Information for intraband contribution). First, in the low-momentum regime, the transition dipole moment exhibits a circular vortex pattern with a spin texture around Dirac nodes (white arrows)<sup>12</sup>. The more efficient coupling of circularly polarized fields with these vortex features is used to explain the enhancement of the relatively low-order harmonics.<sup>5,33,34</sup> Second, in the

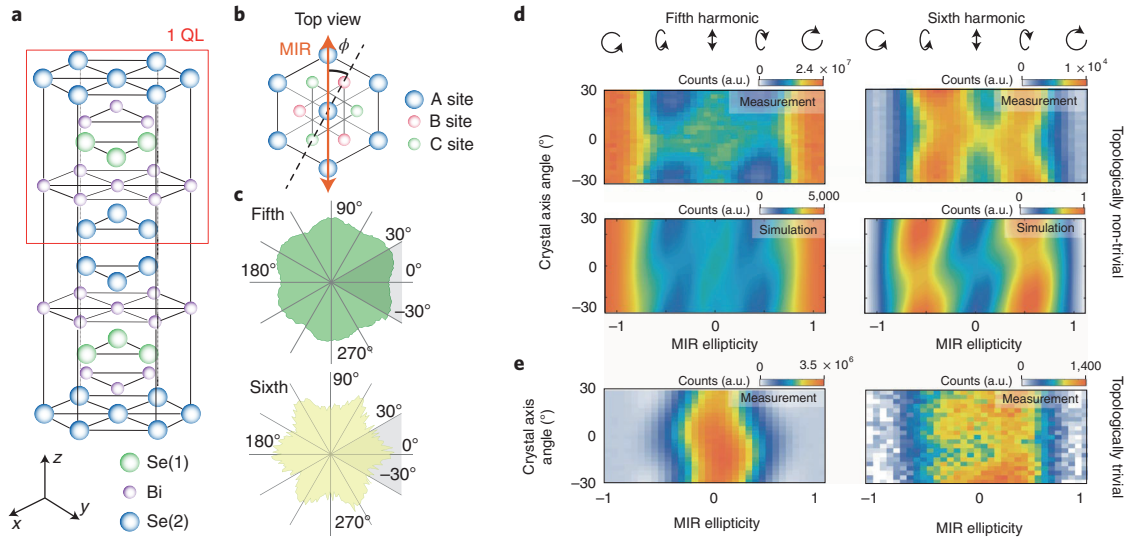


**Fig. 2 | Ellipticity-dependent HHG in topologically trivial and non-trivial materials.** **a**, Crystal structure of  $\text{Bi}_2\text{Se}_3$  with two quintuple layers. One quintuple layer (QL) is highlighted by the red box. **b**, Broken inversion symmetry of the surface layer results in the emission of even- and odd-order harmonics. **c**, Polarization-resolved high-harmonic intensity for the fifth and sixth harmonics. The six-fold pattern directly reflects the symmetry of the interband dipole matrix element and the group velocity (see Supplementary Information). **d**, Measured high-harmonic intensity versus the MIR ellipticity  $\epsilon$  and sample orientation ( $\lambda = 5 \mu\text{m}$ ,  $E_0 = 0.21 \text{ V nm}^{-1}$ ) (top) and the numerically obtained high-harmonic response (bottom). The sample orientation is scanned from  $-30^\circ$  to  $+30^\circ$  (see **c**). The ellipticity is changed from  $\epsilon = -1$  (left-hand circular) to  $\epsilon = 0$  (linear) and  $\epsilon = 1$  (right-hand circular). **e**, Measured high-harmonic intensity versus MIR ellipticity and sample orientation using the topologically trivial sample, which shows a one order of magnitude lower efficiency for linear polarization and no enhancement for circularly polarized excitation.

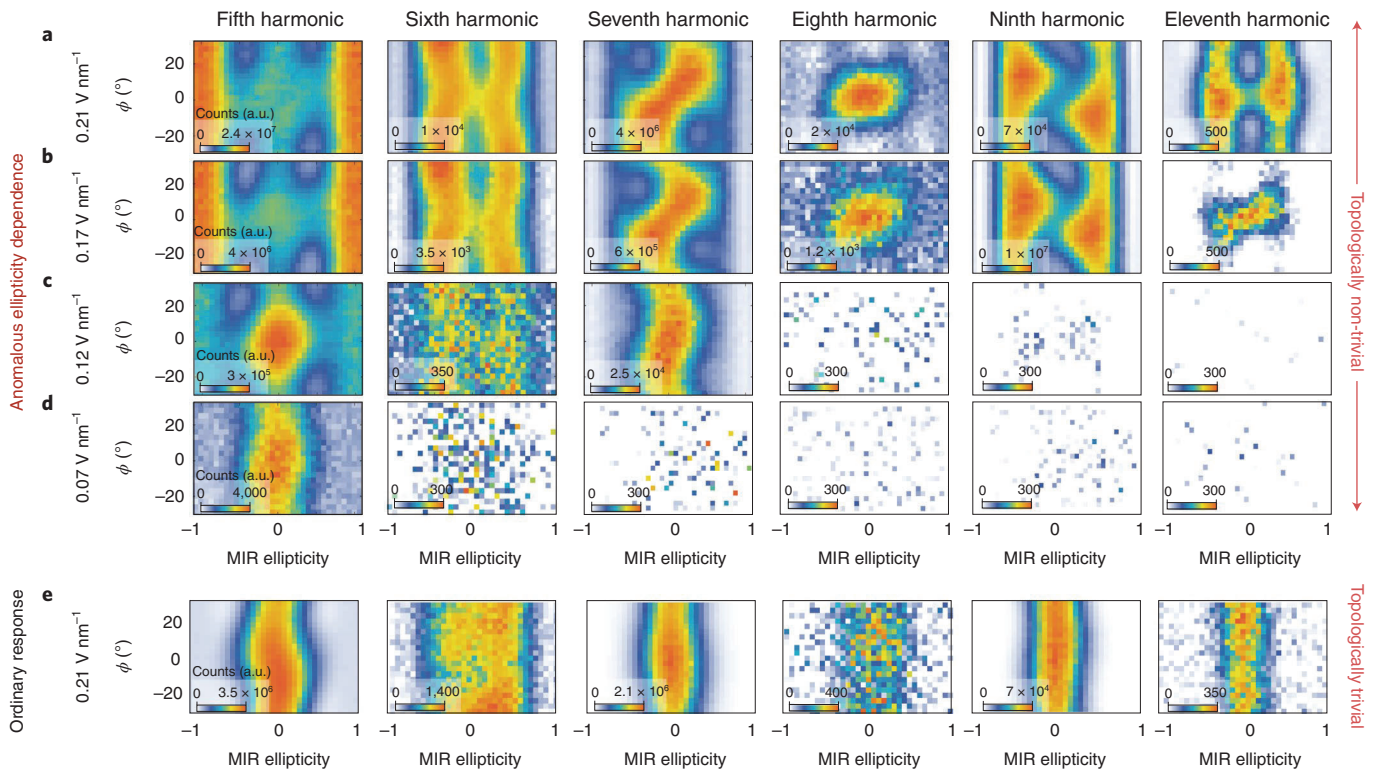


**Fig. 3 | Intensity- and helicity-dependent HHG generation for the topologically trivial and non-trivial samples.** **a-d**, High-harmonic intensity for various MIR ellipticities and crystal axes, measured on the topologically non-trivial  $\text{Bi}_2\text{Se}_3$  sample. Even and odd orders are observed. For decreasing  $E_0$  from  $0.21 \text{ V nm}^{-1}$  (**a**) to  $0.17 \text{ V nm}^{-1}$  (**b**),  $0.12 \text{ V nm}^{-1}$  (**c**) and  $0.07 \text{ V nm}^{-1}$  (**d**) we find the peak field strength needed to probe the topologically protected surface state. At and below this threshold the high-harmonic efficiency is maximized for linear excitation (see **d**). **e**, For the topologically trivial samples neither notable dichroism nor circular enhancement is observed, even for the highest fields strength.

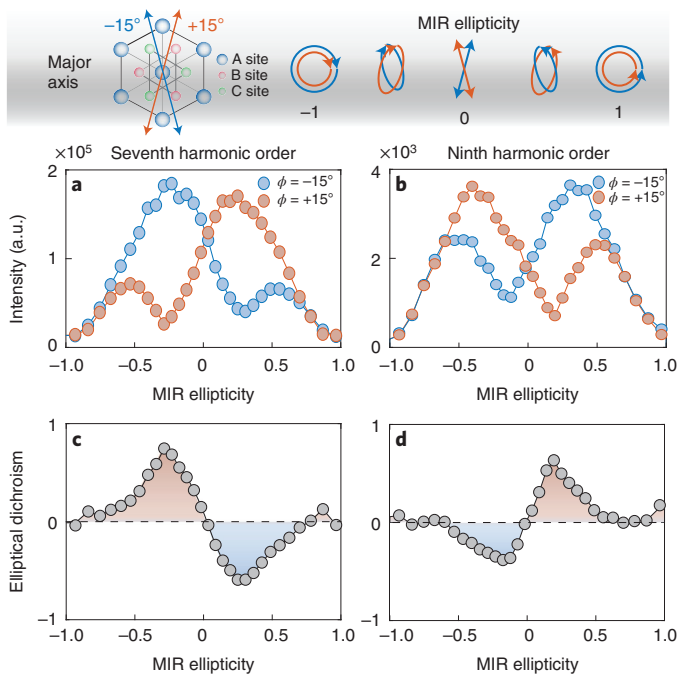


**Fig. 4 | Elliptical dichroism.** Inset: top view of the crystal structure. **a,b**, High-harmonic yield for two crystal orientations of  $\phi = \pm 15^\circ$  for the seventh (**a**) and ninth (**b**) harmonic orders. **c,d** Strong elliptical dichroism is observed for both the seventh (**c**) and ninth (**d**) harmonic orders. Positive ED is shaded in orange, negative ED is shaded in blue.

large-momentum regime, the hexagonal warping, which causes an out-of-plane spin polarization due to strong spin-orbit coupling, increases the high-harmonic response under circular excitation. The out-of-plane component is directly related to the higher-order (third and above) spin-orbit coupling terms in the Hamiltonian (see Supplementary Information and ref. <sup>5</sup>). We note that while the generation for relatively low intensities is dominated by the inter-band channel, at higher intensities both inter- and intra-band channels may contribute<sup>5</sup>.

To further support the interpretation that the circular enhancement arises from the topologically protected surface state, we show in Fig. 3 all measured harmonic orders from the fifth to the eleventh for five field strengths. First, we focus on the fifth harmonic order. For  $E_0 = 0.21 \text{ V nm}^{-1}$ , the ratio of harmonics obtained under circularly polarized excitation versus linearly polarized excitation that is,  $I_{\text{HH,C}}/I_{\text{HH,L}}$  is about  $\mathcal{R} = 1.8$ . Reducing the electric field strength systematically decreases  $\mathcal{R}$  towards an ordinary ellipticity dependence with  $\mathcal{R} < 0.1$ . This electric-field-strength dependence is also expected, since for smaller  $E_0$  values the electrons are not able to probe the high-momentum spin-orbit features attributable to the hexagonal warping (see Fig. 1c for the interband contribution and Supplementary Information for the intraband contributions). Our simulations even reproduce this trend quantitatively (Extended Data Fig. 3). We define an empirically determined threshold field of around  $E_{0,\text{threshold}} = 0.14 \text{ V nm}^{-1}$ , where both the high-harmonic yield obtained for linear and circular excitation are equal ( $\mathcal{R} = 1$ ). Here,  $E_{0,\text{threshold}}$  is a characteristic material parameter related to the strength of the spin-orbit interaction and defines the transition from an ordinary to an anomalous ellipticity dependence in a topologically non-trivial material. Numerical simulations for different wavelengths show that  $E_{0,\text{threshold}}$  is inversely proportional to the driving wavelength  $\lambda$  (see Extended Data Fig. 3). Thus, longer wavelengths in the mid-infrared and terahertz regions are certainly favourable for probing a material's topology without damaging the sample.

Next, we discuss the observed elliptical dichroism. We find different conversion efficiencies for left- and right-elliptically polarized laser fields (at a fixed peak intensity), which becomes most obvious for the seventh and ninth harmonic orders at a crystal angle of  $\phi = \pm 15^\circ$ . For the seventh harmonic, at  $\phi = -15^\circ$ , we observe the highest conversion efficiencies for MIR ellipticities of  $\varepsilon = -0.25$  and the lowest conversion efficiencies for  $\varepsilon = +0.25$ . For the ninth harmonic, we see the reverse trend with helicity, as indicated in Fig. 4. Here we define the elliptical dichroism (ED) as

$$\text{ED} = \frac{2(I_{\phi=+15^\circ} - I_{\phi=-15^\circ})}{\max(I_{\phi=+15^\circ} + I_{\phi=-15^\circ})}$$

where  $I_{\phi=+15^\circ}$  and  $I_{\phi=-15^\circ}$  represent the spectral intensities at crystal angles  $\phi = +15^\circ$  and  $\phi = -15^\circ$ , respectively<sup>35</sup>. For the highest applied field strengths a strong ED value of  $\sim 75\%$  for the seventh harmonic is observed in topologically non-trivial samples. The ED for all measured harmonic orders in the case of the topologically non-trivial sample is shown in the Supplementary Information. For the topologically trivial samples we obtain ED values of  $< 5\%$ .

For the topologically trivial samples, as shown in Fig. 3e, no notable anomalous ellipticity dependence or elliptical dichroism is observed. Similarly, at lower peak intensities, the elliptical dichroism and anomalous dependence vanish (Fig. 3d). Thus, we conclude that the observed elliptical dichroism is a signature of the topologically protected surface state, as also evident in earlier photoemission spectroscopy studies<sup>36</sup>.

A particular strength of high-harmonic spectroscopy is its potential to study topological phase transitions with high time resolution. Such phase transitions can be induced via ultrafast excitation, such as with strong terahertz fields, as seen in  $\text{WTe}_2$  (ref. <sup>37</sup>). Recent theoretical developments include the Floquet engineering of topological states using strong circularly polarized laser fields<sup>38</sup> and the possibility of transient non-trivial topological states in transition metal dichalcogenides<sup>39</sup>. Probing these non-equilibrium states and their dynamics calls for a high time resolution. This can be achieved even down to subcycle timescales via the attosecond synchronization of high harmonics with the driving laser pulses.

In conclusion, we have demonstrated an all-optical method based on HHG using a circularly polarized strong MIR laser field to probe distinct topological phases, the non-trivial topologically protected surface states of pristine  $\text{Bi}_2\text{Se}_3$ , and the trivial state after chemical doping. We identify a threshold field strength of the laser required to probe this phase transition, which motivates the use of long laser wavelengths. Our interpretation of the enhanced generation efficiency and elliptical dichroism for the non-trivial topological phase is corroborated by a theoretical treatment based on a pair of valence and conduction bands of the topological surface state. The more conventional and relatively inefficient response from the doped sample is reproduced by simulating the HHG process in the bulk bands only. Our results advance the understanding of HHG physics in topological materials and lay the foundation for novel strong-field chiral physics, which includes the possible realization of ultrafast helical currents on the surfaces of topological materials.

### Online content

Any methods, additional references, Nature Research reporting summaries, source data, extended data, supplementary information, acknowledgements, peer review information; details of author contributions and competing interests; and statements of data and code availability are available at <https://doi.org/10.1038/s41566-022-01050-7>.

Received: 24 November 2021; Accepted: 26 June 2022;  
Published online: 18 August 2022

## References

1. Zhang, H. et al. Topological insulators in  $\text{Bi}_2\text{Se}_3$ ,  $\text{Bi}_2\text{Te}_3$  and  $\text{Sb}_2\text{Te}_3$  with a single Dirac cone on the surface. *Nat. Phys.* **5**, 438–442 (2009).
2. Moore, J. E. The birth of topological insulators. *Nature* **464**, 194–198 (2010).
3. Hasan, M. Z. & Kane, C. L. Colloquium: Topological insulators. *Rev. Mod. Phys.* **82**, 3045–3067 (2010).
4. Roushan, P. et al. Topological surface states protected from backscattering by chiral spin texture. *Nature* **460**, 1106–1109 (2009).
5. Baykuseva, D. et al. Strong-field physics in three-dimensional topological insulators. *Phys. Rev. A* **103**, 023101 (2021).
6. Brahlek, M. et al. Topological-metal to band-insulator transition in topological-metal to band-insulator transition in  $(\text{Bi}_{1-x}\text{In}_x)_2\text{Se}_3$ . *Phys. Rev. Lett.* **109**, 186403 (2012).
7. Salehi, M. et al. Finite-size and composition-driven topological phase transition in  $(\text{Bi}_{1-x}\text{In}_x)_2\text{Se}_3$  thin films. *Nano Lett.* **16**, 5528–5532 (2016).
8. Chen, Y. L. et al. Experimental realization of a three-dimensional topological insulator,  $\text{Bi}_2\text{Te}_3$ . *Science* **325**, 178–181 (2009).
9. Xia, Y. et al. Observation of a large-gap topological-insulator class with a single Dirac cone on the surface. *Nat. Phys.* **5**, 398–402 (2009).
10. Fu, L. Hexagonal warping effects in the surface states of the topological insulator  $\text{Bi}_2\text{Te}_3$ . *Phys. Rev. Lett.* **103**, 266801 (2009).
11. Boolakee, T. Light-field control of real and virtual charge carriers. *Nature* **605**, 251–255 (2022).
12. Xu, S.-Y. et al. Topological phase transition and texture inversion in a tunable topological insulator. *Science* **332**, 560–564 (2011).
13. Wu, L. et al. Quantized Faraday and Kerr rotation and axion electrodynamics of a 3D topological insulator. *Science* **354**, 1124–1127 (2016).
14. Ali, M. N. & Parkin, S. S. P. Butterfly magnetoresistance, quasi-2D Dirac Fermi surface and topological phase transition in  $\text{ZrSiS}$ . *Sci. Adv.* **2**, e1601742 (2016).
15. Zhang, A. et al. Topological phase transition between distinct Weyl semimetal states in  $\text{MoTe}_2$ . *Phys. Rev. B* **100**, 201107(R) (2019).
16. Sobota, J. A., He, Y. & Shen, Z. X. Angle-resolved photoemission studies of quantum materials. *Rev. Mod. Phys.* **93**, 025006 (2021).
17. Corkum, P. B. B. & Krausz, F. Attosecond science. *Nat. Phys.* **3**, 381–387 (2007).
18. Itatani, J. et al. Tomographic imaging of molecular orbitals. *Nature* **432**, 867–871 (2004).
19. You, Y. S., Reis, D. A. & Ghimire, S. Anisotropic high-harmonic generation in bulk crystals. *Nat. Phys.* **13**, 345–349 (2017).
20. Lakhota, H. et al. Laser picoscopy of valence electrons in solids. *Nature* **583**, 55–59 (2020).
21. Vampa, G. et al. All-optical reconstruction of crystal band structure. *Phys. Rev. Lett.* **115**, 193603 (2015).
22. Liu, H. et al. High-harmonic generation from an atomically thin semiconductor. *Nat. Phys.* **13**, 262–265 (2017).
23. Luu, T. T. & Wörner, H. J. Measurement of the Berry curvature of solids using high-harmonic spectroscopy. *Nat. Commun.* **9**, 916 (2018).
24. Bauer, D. & Hansen, K. K. High-harmonic generation in solids with and without topological edge states. *Phys. Rev. Lett.* **120**, 177401 (2018).
25. Silva, R. E. F., Jiménez-Galán, Á., Amorim, B., Smirnova, O. & Ivanov, M. Topological strong-field physics on sub-laser-cycle timescale. *Nat. Photonics* **13**, 849–854 (2019).
26. Chacón, A. et al. Circular dichroism in higher-order harmonic generation: heralding topological phases and transitions in chern insulators. *Phys. Rev. B* **102**, 134115 (2020).
27. Bai, Y. et al. High-harmonic generation from topological surface states. *Nat. Phys.* **17**, 311–315 (2020).
28. Schmid, C. P. et al. Tunable non-integer high-harmonic generation in a topological insulator. *Nature* **593**, 385–390 (2021).
29. Baykuseva, D. & Ghimire, S. All-optical probe of three-dimensional topological insulators based on high-harmonic generation by circularly polarized laser fields. *Nano Lett.* **21**, 8970–8978 (2021).
30. Hsieh, D. et al. Nonlinear optical probe of tunable surface electrons on a topological insulator. *Phys. Rev. Lett.* **106**, 057401 (2011).
31. Vampa, G., Liu, H., Heinz, T. F. & Reis, D. A. Disentangling interface and bulk contributions to high-harmonic emission from solids. *Optica* **6**, 553 (2019).
32. Neufeld, O., Podolsky, D. & Cohen, O. Floquet group theory and its application to selection rules in harmonic generation. *Nat. Commun.* **10**, 405 (2019).
33. Yoshikawa, N., Tamaya, T. & Tanaka, K. High-harmonic generation in graphene enhanced by elliptically polarized light excitation. *Science* **356**, 736–738 (2017).
34. Feng, Y. et al. Semiclassical analysis of ellipticity dependence of harmonic yield in graphene. *Phys. Rev. A* **104**, 043525 (2021).
35. Baykuseva, D. & Wörner, H. J. Chiral discrimination through bielliptical high-harmonic spectroscopy. *Phys. Rev. X* **8**, 031060 (2018).
36. Neupane, M. & Hasan, M. Z. Oscillatory surface dichroism of the insulating topological insulator  $\text{Bi}_2\text{Te}_3$ . *Phys. Rev. B* **88**, 165129 (2013).
37. Sie, E. J. et al. An ultrafast symmetry switch in a Weyl semimetal. *Nature* **565**, 61–66 (2019).
38. Hübener, H., Sentef, M. A., Giovannini, U. D., Kemper, A. F. & Rubio, A. Creating stable Floquet–Weyl semimetals by laser-driving of 3D Dirac materials. *Nat. Commun.* **8**, 13940 (2017).
39. Jiménez-Galán, Á., Silva, R. E. F., Smirnova, O. & Ivanov, M. Lightwave control of topological properties in 2D materials for sub-cycle and non-resonant valley manipulation. *Nat. Photonics* **14**, 728–732 (2020).

**Publisher's note** Springer Nature remains neutral with regard to jurisdictional claims in published maps and institutional affiliations.

Springer Nature or its licensor holds exclusive rights to this article under a publishing agreement with the author(s) or other rightsholder(s); author self-archiving of the accepted manuscript version of this article is solely governed by the terms of such publishing agreement and applicable law.

© The Author(s), under exclusive licence to Springer Nature Limited 2022

## Data availability

Data underlying the results presented in this paper are not publicly available at this time, but may be obtained from the authors upon request.

## Acknowledgements

This work is primarily supported by the US Department of Energy, Office of Science, Office of Basic Energy Sciences, Chemical Sciences, Geosciences, and Biosciences Division through the AMOS program. Use of the Stanford Synchrotron Radiation Lightsource, SLAC National Accelerator Laboratory, is supported by the US Department of Energy, Office of Science, Office of Basic Energy Sciences under Contract No. DE-AC02-76SF00515. C.H. acknowledges support from the Humboldt Fellowship and the W. M. Keck Foundation. Y.K. acknowledges the Urbanek–Chorodow Fellowship from Stanford University. D.R.B. acknowledges support from the Swiss National Science Foundation (SNSF) through projects P2E2P2\_184255 and P400P2\_194343. D.J. and S.O. are supported by National Science Foundation's DMR2004125 and MURI W911NF2020166. J.A.S., M.H. and P.S.K. were supported by the Department of Energy, Office of Basic Energy Sciences, Division of Materials Science and Engineering. Theoretical calculations were performed using the Sherlock HPC cluster at Stanford University. We thank Alexis Chacón and Fang Liu for fruitful discussions.

## Author contributions

C.H., Y.K. and S.G. conceived the project. C.H. and Y.K. designed the setup. C.H. and Y.K. performed the experiments and analysed the data. T.F.H., D.A.R. and S.G. supervised the project. D.R.B. developed the theoretical model and performed the numerical calculations. D.J. and S.O. synthesized and characterized the samples. C.H., M.H. and J.A.S. performed the ARPES measurements at SSRL. All authors contributed to the interpretation of data.

## Competing interests

The authors declare no competing interests.

## Additional information

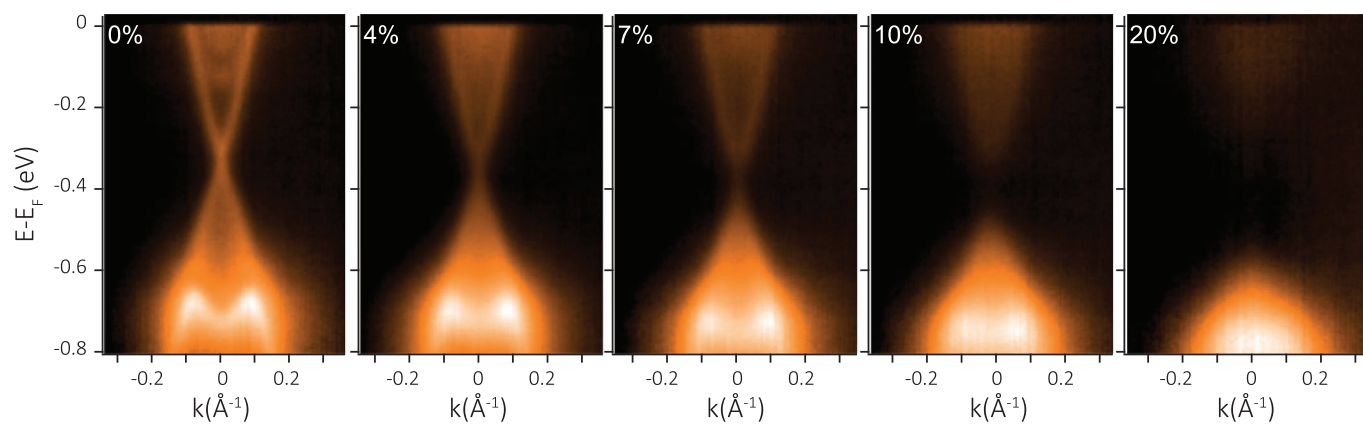
**Extended data** is available for this paper at <https://doi.org/10.1038/s41566-022-01050-7>.

**Supplementary information** The online version contains supplementary material available at <https://doi.org/10.1038/s41566-022-01050-7>.

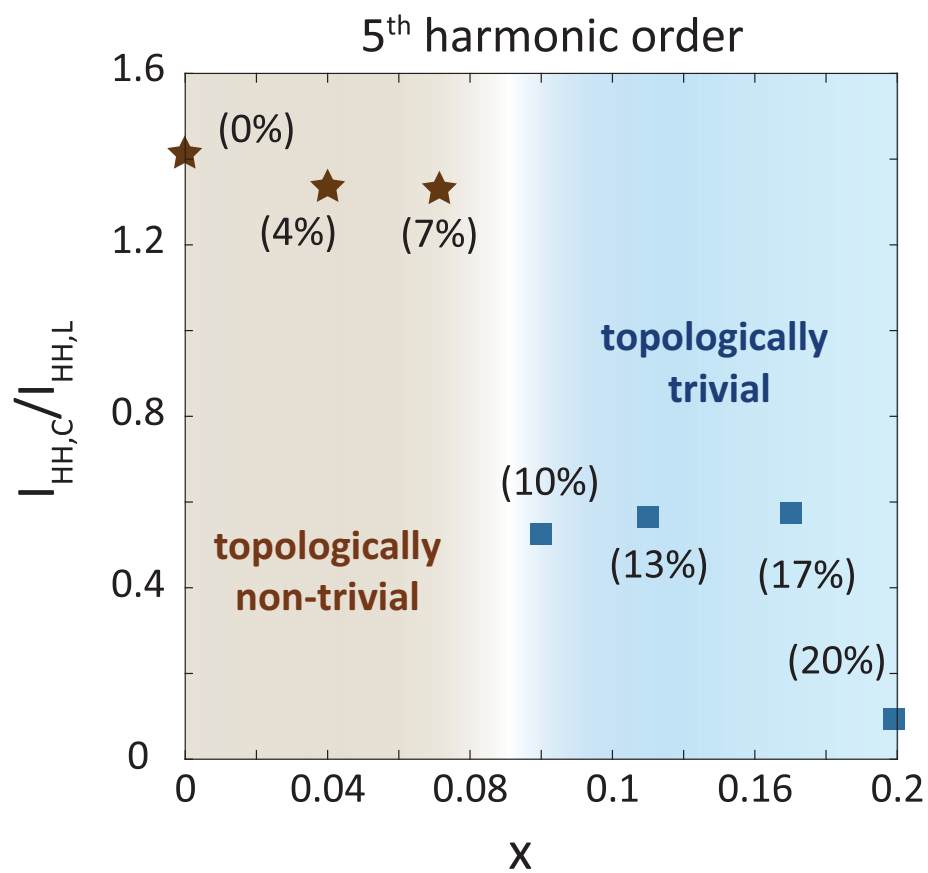
**Correspondence and requests for materials** should be addressed to Christian Heide or Shambhu Ghimire.

**Peer review information** *Nature Nanotechnology* thanks Dieter Bauer and the other, anonymous, reviewer(s) for their contribution to the peer review of this work.

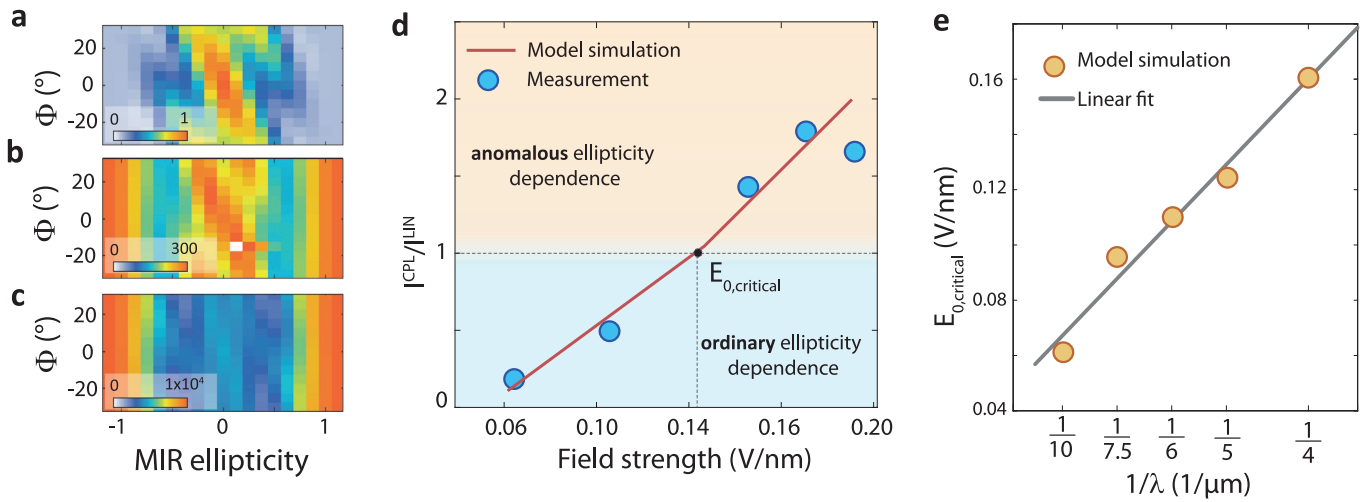
**Reprints and permissions information** is available at [www.nature.com/reprints](http://www.nature.com/reprints).



**Extended Data Fig. 1 | ARPES measurements.** ARPES measurements of  $\text{Bi}_2\text{Se}_3$  for 5 different indium concentrations.



**Extended Data Fig. 2 | Topological phase transition.** Ratio of HH yield for circular vs. linear excitation for various indium concentrations  $x$ . Measurements are performed at peak field  $E_0 = 0.15$  V/nm.



**Extended Data Fig. 3 | Transition from ordinary to anomalous ellipticity dependence.** **a, b, c**, Simulations of crystal orientation and MIR ellipticity dependent HH yield for three different field strengths  $E_0 = 0.06, 0.14, 0.25$  V/nm. **d**, The ratio between HH obtained under circular and linear excitation for  $\Phi = 0$  is shown for various field strengths. The blue filled dots are the experimentally obtained values, the red line represents values from the simulation. The threshold field strength  $E_{0,threshold}$  is defined when this ratio becomes 1. **e**, The threshold field scales inversely with the wavelengths.